

A new surface-tension formulation for multi-phase SPH using a reproducing divergence approximation

S. Adami *, X.Y. Hu, N.A. Adams

Institute of Aerodynamics, Technische Universität München, 85748 Garching, Germany

ARTICLE INFO

Article history:

Received 26 June 2009

Received in revised form 5 February 2010

Accepted 16 March 2010

Available online 18 March 2010

Keywords:

Multi-phase flows

Surface tension

Particle method

ABSTRACT

In this paper, we propose a new surface-tension formulation for multi-phase smoothed particle hydrodynamics (SPH). To obtain a stable and accurate scheme for surface curvature, a new reproducing divergence approximation without the need for a matrix inversion is derived. Furthermore, we introduce a density-weighted color-gradient formulation to reflect the reality of an asymmetrically distributed surface-tension force. We validate our method with analytic solutions and demonstrate convergence for different cases. Furthermore, we show that our formulation can handle phase interfaces with density and viscosity ratios of up to 1000 and 100, respectively. Finally, complex three-dimensional simulations including breakup of an interface demonstrate the capabilities of our method.

© 2010 Elsevier Inc. All rights reserved.

1. Introduction

Surface-tension effects are important for many multi-phase flow phenomena. Especially when the characteristic length scales of the investigated system are sufficiently small, the surface-tension forces become relevant compared to inertia effects and affect the flow field. Many industrial applications include multi-phase flow systems and encounter problems such as drop deformation and breakup in rather simple shear flows, wetting effects or Marangoni-force driven motion of interfaces. Therefore the accurate simulation of flows with complex interfaces is an interesting problem with practical relevance and motivates our work.

There are mainly two approaches for the numerical solution of the governing equations of the flow system, either using a grid-based method with a Eulerian formulation or a meshless method from a Lagrangian point of view. In this paper, we employ smoothed particle hydrodynamics (SPH) [10] due to its conceptual advantages for modeling of complex multi-phase flows. With this Lagrangian particle method, material interfaces are represented self-adaptively without the need for complex interface-capturing or front-tracking algorithms. By the use of a color function each particle is assigned to a single phase throughout a simulation. In doing so, interfaces can easily be followed and strong deformations and even breakup can be handled.

With SPH there are generally two ways to model the surface-tension effect: one is based on microscopic inter-phase attractive potentials [13,16]; the other one is based on a macroscopic surface-tension model [11,6]. Although the implementation of an inter-phase attractive potential is straightforward, one of the difficulties is that the resulting surface tension needs to be calibrated. Furthermore, with given parameters, the surface tension is resolution-dependent and does not converge to a fixed value with increasing resolution. On the other hand, the approach using a macroscopic surface-tension model recovers the prescribed surface tension and converges to the exact value with increasing resolution. Usually, this model is implemented in SPH by the continuum surface force (CSF) method of Brackbill et al. [1]. In this method, a color function is used to describe different phases, and the interface is defined as a finite transitional band, where the color gradient does not vanish. Within this band, the surface tension is approximated as a continuous force.

* Corresponding author.

E-mail address: stefan.adami@aer.mw.tum.de (S. Adami).

The surface-tension model for multi-phase SPH of Morris [11] uses a smoothed color function and has difficulties in predicting the surface curvature, i.e. the divergence of the unit interface-normal direction. One difficulty arises from the fact, that the standard SPH approximation of the divergence requires full support of the kernel function, which cannot be satisfied within the transitional band. Another problem is the color gradient near the edge of the transition band, which has small magnitude and may lead to an erroneous direction. In the work of Hu and Adams [6] a sharp color function with a discontinuity at the interface is used directly. The calculation of the surface curvature is circumvented by introducing a surface-stress tensor which only depends on the color gradient. Furthermore, since the magnitude of the surface-stress tensor is proportional to the magnitude of the color gradient, the contribution of a small color gradient vanishes hence does not introduce numerical difficulties.

In realistic configurations the surface force may not be distributed uniformly on each side of the interface. For example at an air–water interface, the surface force is dominantly acting on the water side. In all current approaches the surface force modeled by SPH is assumed to be distributed uniformly across the interface. Not only being nonphysical, this assumption can also introduce numerical problems. For example, in an air–water interface flow the surface force on the air side can introduce an acceleration about 1000 times higher than that on the water side. Consequentially, the stiffness of the equation of motion increases dramatically, and the step-size for time integration is strongly limited.

In this work, we revisit the formulation of surface curvature based on a sharp color function. To obtain a stable and accurate surface-curvature calculation without full support of the kernel function, a new reproducing divergence approximation is derived. Unlike previous formulations, which calculate the divergence from reproducing gradient approximations, the new approximation does not require a matrix inversion. Furthermore, we have not found notable effects caused by the errors due to small color-gradient values at the fringes of the transitional band. To reflect the reality of non-uniformly distributed surface forces, a new density-weighted color-gradient formulation is used. Several numerical tests on static water drops, oscillating drops, drop deformation and splitting in shear flow are carried out to demonstrate the potential of the present method. The results show that we achieve a comparable accuracy as with the formulation of Hu and Adams [6]. But as we can relax the dominating surface-tension based time-step criterion in the lighter phase, the computational effort of our new formulation is significantly smaller, especially for problems with large density ratios.

2. Governing equations

The isothermal Navier–Stokes equations are solved in a moving Lagrangian frame

$$\frac{d\rho}{dt} = -\rho \nabla \cdot \mathbf{v}, \quad (1)$$

$$\frac{d\mathbf{v}}{dt} = \mathbf{g} + \frac{1}{\rho} [-\nabla p + \mathbf{F}^{(v)} + \mathbf{F}^{(s)}], \quad (2)$$

where ρ , p , \mathbf{v} and \mathbf{g} are material density, pressure, velocity and body force, respectively. $\mathbf{F}^{(v)}$ denotes the viscous force and $\mathbf{F}^{(s)}$ is the interfacial surface force.

With SPH incompressible flow is usually modeled by the weakly-compressible approach in which a stiff EOS is used to relate the pressure to the density, i.e.

$$p = p_0 \left[\left(\frac{\rho}{\rho_0} \right)^\gamma - 1 \right] + \chi, \quad (3)$$

with $\gamma = 7$, the reference pressure p_0 , the reference density ρ_0 and the background pressure χ . These parameters and the artificial speed of sound are chosen following a scale analysis presented by Morris et al. [12] which limits the threshold of the admissible density variation usually to 1%.

The viscous force $\mathbf{F}^{(v)}$ simplifies to the incompressible formulation

$$\mathbf{F}^{(v)} = \eta \nabla^2 \mathbf{v}, \quad (4)$$

where η is the dynamic viscosity. Following the CSF model of Brackbill et al. [1] for constant surface tension, the surface force can be expressed as a volumetric force using the surface delta function δ_Σ by

$$\mathbf{F}^{(s)} = -\alpha \kappa \mathbf{n} \delta_\Sigma. \quad (5)$$

The capillary force $\alpha \kappa \mathbf{n} \delta_\Sigma$ is calculated with the curvature κ , the normal vector of the interface \mathbf{n} and the surface-delta function δ_Σ . This expression describes the pressure-jump condition normal to an interface. In this work we focus only on the case where the interfacial surface tension is constant. Hence, the Marangoni force $\nabla_\Sigma \alpha \delta_\Sigma$ has no influence on the interface dynamics since the interfacial gradient of the surface tension $\nabla_\Sigma \alpha$ is zero.

3. Numerical method

The governing equations are discretized by the multi-phase SPH method presented in Hu and Adams [6]. Each particle represents a Lagrangian element of fluid, carrying all local phase properties. With updating the positions of the particles this

method accounts for advection as the governing equations are formulated in terms of material derivatives. For implementation we employ the Parallel Particle-Mesh (PPM) Library [15] which allows for large-scale particle simulations on parallel computer architectures.

3.1. Multi-phase flow solver

According to Hu and Adams [6] we calculate the density of a particle i at each time-step from a summation over all neighboring particles j

$$\rho_i = m_i \sum_j W_{ij} = \frac{m_i}{V_i}. \quad (6)$$

Here, m_i denotes the particle mass, $W_{ij} = W(\mathbf{r}_i - \mathbf{r}_j, h)$ is a kernel function with smoothing length h , and V_i is the volume of particle i . This summation allows for density discontinuities and conserves mass exactly.

The interpolation kernel function W can be any function which satisfies

$$\int W(\mathbf{r}, h) d\mathbf{r} = 1 \quad (7)$$

and has the Dirac delta-function property

$$\lim_{h \rightarrow 0} W(\mathbf{r}, h) = \delta(\mathbf{r}). \quad (8)$$

Furthermore, according to Monaghan [10] a suitable kernel function should also have compact support to allow for numerically efficient approximations of the field quantities and gradients. Here, we use the quintic spline function presented by Morris et al. [12] with a compact support of $3h$. This kernel satisfies the above mentioned criteria, and Hongbin and Xin [5] showed that among 10 proposed kernels the quintic spline function or the Gaussian function are favorable in terms of computational accuracy.

The pressure term in the momentum equation is approximated as

$$\frac{d\mathbf{v}_i^{(p)}}{dt} = -\frac{1}{\rho_i} \nabla p_i = -\frac{1}{m_i} \sum_j (V_i^2 + V_j^2) \tilde{p}_{ij} \frac{\partial W}{\partial \mathbf{r}_{ij}} \mathbf{e}_{ij}, \quad (9)$$

with the weight-function gradient $\frac{\partial W}{\partial \mathbf{r}_{ij}} \mathbf{e}_{ij} = \nabla W(\mathbf{r}_i - \mathbf{r}_j)$ and the inter-particle pressure

$$\tilde{p}_{ij} = \frac{\rho_i p_j + \rho_j p_i}{\rho_i + \rho_j}. \quad (10)$$

In the case of interacting particles of the same phase this form of \tilde{p}_{ij} recovers the simple midpoint-averaged pressure between the two particles. But when two particles of different phases interact, the density-weighted inter-particle pressure from Eq. (10) ensures that $\nabla p / \rho$ is continuous even for a discontinuous density field, see [8].

The viscous force is derived from the inter-particle-averaged shear stress with a combined viscosity. A simplification for incompressible flows gives

$$\frac{d\mathbf{v}_i^{(v)}}{dt} = v_i \nabla^2 \mathbf{v}_i = \frac{1}{m_i} \sum_j \frac{2\eta_i \eta_j}{\eta_i + \eta_j} (V_i^2 + V_j^2) \frac{\mathbf{v}_{ij}}{r_{ij}} \frac{\partial W}{\partial \mathbf{r}_{ij}}, \quad (11)$$

where $v_i = \eta_i / \rho_i$ is the local kinematic viscosity of particle i , $\mathbf{v}_{ij} = \mathbf{v}_i - \mathbf{v}_j$ is the relative velocity of particle i and j and $r_{ij} = |\mathbf{r}_i - \mathbf{r}_j|$ is the distance of the two particles. This form of the viscous force conserves linear momentum. Angular conservation can be achieved using other formulations such as presented by Hu and Adams [7].

To distinguish between particles of different phases we use integer identifiers. Without a phase transition model this identifier is constant for a particle i during the entire simulation and is advected with the flow field. Introducing special interactions between particles of different phases, interface effects are incorporated within our method adaptively without the need of special interface reconstruction schemes. Therefore we can handle arbitrary interface shapes as well as breakup or merging of phases.

To calculate surface-tension forces between particles of different phases we introduce a color function c as

$$c_l^k = \begin{cases} 1, & \text{if the } k\text{th particle does not belong to the phase of particle } l, \\ 0, & \text{if the } k\text{th particle belongs to the phase of particle } l. \end{cases} \quad (12)$$

This color function has a unit-jump at a phase interface. Consequently, the gradient of the color function has a delta-function-like distribution and gives an approximation of the surface-delta function δ_z in Eq. (5). Furthermore, the normal direction at the interface can be obtained from the color gradient by

$$\mathbf{n} = \frac{\nabla c}{|\nabla c|}. \quad (13)$$

To further illustrate the transition region with a non-zero color gradient and the normal direction, Fig. 1 shows a sketch of the particles near an interface with the surface-delta function δ_Σ .

In this work, we do not use the color-gradient formulation of Hu and Adams [6], but introduce a new density-weighted summation. Physically, at an air–water interface the surface-tension forces in the liquid phase are much more prominent than those in the gas phase. Consequently, the interfacial motion is mainly driven by the water phase. Reflecting this behavior, we formulate the gradient of the color function as

$$\nabla c_i = \frac{1}{V_i} \sum_j [V_i^2 + V_j^2] \tilde{c}_{ij} \frac{\partial W}{\partial r_{ij}} \mathbf{e}_{ij} \quad (14)$$

using the inter-particle average

$$\tilde{c}_{ij} = \frac{\rho_j}{\rho_i + \rho_j} c_i^i + \frac{\rho_i}{\rho_i + \rho_j} c_j^j. \quad (15)$$

Note that for a density ratio $\Phi_\rho = \rho_1/\rho_2 = 1$ between the two phases, this expression is equal to the midpoint average of two particles i and j of Hu and Adams [6]. Fig. 2(a) shows the situation when two particles of different phase but with the same density interact. Here, the surface-delta function is symmetric since $\tilde{c}_{ij} = \tilde{c}_{ji} = 0.5$. For density ratios Φ_ρ different from one the density-weighted inter-particle average Eq. (15) leads to a discontinuous color gradient as shown in Fig. 2(b).

It is important to note, that with the assumption of incompressibility of both phases and given the fact that $\tilde{c}_{ij} + \tilde{c}_{ji} = 1$, this new color gradient distribution maintains the property

$$\int_{-\infty}^{+\infty} \delta_\Sigma(\mathbf{r}) d\mathbf{r} = \int_{-\infty}^{+\infty} |\nabla c(\mathbf{r})| d\mathbf{r}, \quad (16)$$

thus we can replace the surface-delta function in the surface-force term, Eq. (5), with the weighted color gradient, Eq. (14). In doing so, the resulting surface-tension force distribution along the interface is physically more sensible than for previous approaches.

To calculate the interface curvature within the transition band, we present a new reproducing divergence approximation without the need for the full support of the kernel function to be contained in the transition band. Starting from a Taylor series of a continuous vector field φ about the i th particle, we multiply the equation with the gradient of the kernel function

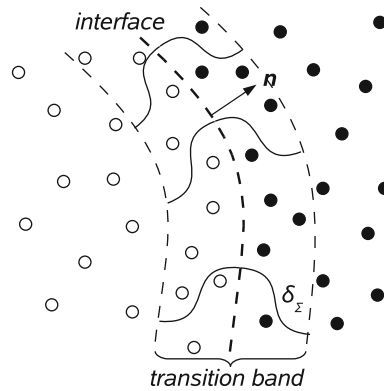


Fig. 1. Sketch of the transition band at an interface with the surface delta function δ_Σ , the normal \mathbf{n} and particles of two different phases.

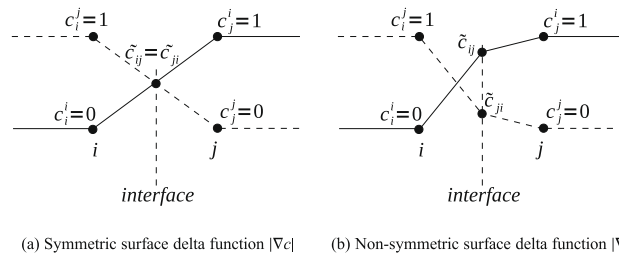


Fig. 2. Sketch of the color function and surface-delta function between two particles i and j of different phases with density ratio (a) $\rho_i/\rho_j = 1$ and (b) $\rho_i/\rho_j \gg 1$.

and integrate over the entire domain. Neglecting second and higher order terms, we obtain the summation form of the corrected gradient as

$$\nabla \varphi_i = \left[\sum_j \varphi_{ji} \otimes \nabla W(\mathbf{r}_{ji}) V_j \right] \left[\sum_j \mathbf{r}_{ji} \otimes \nabla W(\mathbf{r}_{ji}) V_j \right]^{-1}. \quad (17)$$

This formulation is very similar to the reproducing gradient approximation of Chen et al. [2]. One way to obtain the reproducing divergence approximation is to take the trace of Eq. (17). But since the denominator is a $d \times d$ matrix, where d is the number of spatial dimensions, this matrix must first be constructed and then inverted. To avoid this additional computational work, we further approximate the denominator of the formulation given above by two identities presented in Español and Revenga [3]

$$\int \mathbf{r} \otimes \nabla W(\mathbf{r}) d\mathbf{r} = -\mathbf{I}, \quad \int \mathbf{r} \cdot \nabla W(\mathbf{r}) d\mathbf{r} = -d \quad (18)$$

with \mathbf{I} being the unit matrix, as

$$\sum_j \mathbf{r}_{ji} \otimes \nabla W(\mathbf{r}_{ji}) V_j \approx \frac{\mathbf{I}}{d} \left(\sum_j \mathbf{r}_{ji} \cdot \nabla W(\mathbf{r}_{ji}) V_j \right). \quad (19)$$

Combining Eqs. (17) and (19) and taking the trace, we find that the approximated divergence can be written as

$$\nabla \cdot \varphi_i = d \frac{\sum_j \varphi_{ij} \cdot \mathbf{e}_{ij} \frac{\partial W}{\partial r_{ij}} V_j}{\sum_j r_{ij} \frac{\partial W}{\partial r_{ij}} V_j}. \quad (20)$$

Now only two simple summations are required to approximate the divergence for a particle i . Furthermore, for a linear field $\varphi = A\mathbf{r}$ with A being a constant, Eq. (20) gives Ad , hence reproduces the divergence of a linear field. Note, that Eq. (20) reproduces the divergence even when there is no full support of the kernel function of a particle contained within the transition band.

Using the above formulation to calculate the curvature of the interface, i.e. the divergence of the interface-normal direction, we finally obtain the acceleration of an interface particle by surface tension as

$$\frac{d\mathbf{v}_i^{(s)}}{dt} = -\frac{\alpha_i}{m_i} \kappa_i \nabla c_i. \quad (21)$$

Unlike the formulation in Hu and Adams [6] Eq. (21) takes effect as a body force, hence does not exactly conserve the total momentum of the system. Note, that when the density ratio Φ_ρ at the interface is large, according to Eq. (14) the surface force on the heavier phase is Φ_ρ -times of that on the lighter phase, thus both phases obtain accelerations with the same magnitude.

3.2. Time-step criteria

The equations presented above are integrated in time with the velocity Verlet scheme. For stability reasons the maximum time-step is chosen based on several time-step criteria [10,18]. Within the weakly-compressible SPH formulation, the time-step must satisfy the CFL-condition based on the maximum artificial sound speed and the maximum flow speed

$$\Delta t \leq 0.25 \frac{h}{c_{\max} + |u_{\max}|}, \quad (22)$$

the viscous condition

$$\Delta t \leq 0.125 \frac{h^2}{\nu}, \quad (23)$$

the body force condition

$$\Delta t \leq 0.25 \left(\frac{h}{|\mathbf{g}|} \right)^{1/2}, \quad (24)$$

and the surface-tension condition

$$\Delta t \leq 0.25 \left(\frac{\rho h^3}{2\pi\alpha} \right)^{1/2}. \quad (25)$$

For satisfying all conditions the global time-step is taken as minimum of Eqs. (22)–(25). Note that the surface-tension condition for the time-step constraint is based on the reference density. Hence, the admissible step-size of the time integration for a surface-tension dominated flow problem can be much larger than obtained with the formulation of Hu and Adams [6].

4. Numerical examples

In the following section we validate our surface-tension model by comparison to analytic solutions of two-dimensional problems for steady and unsteady problems. We demonstrate the capabilities of our method by simulating the breakup of a three-dimensional drop in a shear flow. For all cases we use ghost particles to impose the boundary conditions, see [14]. The mirror-particle technique is well suited for simple geometries with straight walls and allows for symmetry and no-slip conditions. Except for the last numerical example we use symmetry conditions at the boundaries and enforce a Neumann boundary condition for the pressure. Additionally, for walls we adjust the velocity of a mirrored ghost wall particle to

$$\mathbf{v}_{\text{virtual}} = 2\mathbf{v}_{\text{wall}} - \mathbf{v}_{\text{real}}.$$

4.1. Square-droplet deformation

In our first test, we investigate the surface-tension driven deformation of an initially square droplet. We place a square patch of fluid “1” with an edge length of $l_x = l_y = 0.6$ into a box of fluid “2” with a domain size of $L_x = L_y = 1$. The density of both phases is $\rho = 1$, and we use a dynamic viscosity of $\eta = 0.2$. The surface-tension coefficient is set to $\alpha = 1$. Fig. 3(a) shows the initial particle positions of the two fluids of same density. After $t = 1$ a circular droplet is formed and the particles are at rest, see Fig. 3(b).

From the Laplace-law we find that the pressure within the droplet must be higher than that of the surrounding fluid. In two-dimensions the pressure drop across the interface must satisfy the condition

$$\Delta p = \frac{\alpha}{R} = \frac{\alpha\sqrt{\pi}}{l_x}, \quad (26)$$

where R is the final radius of the drop. In Fig. 4(a) the pressure profiles of two different initial square droplets of size $l_x = 0.4$ and 0.6 each with two different resolutions ($3h = 0.06$ and 0.03) are plotted against the radial coordinate. The dotted lines represent the analytic solutions for the two cases. The calculated pressure profiles agree well with the Laplace-law and convergence is demonstrated for both cases. Note also the thinning of the transition region at the interface with increasing resolution.

For our non-conservative surface-tension formulation we expect good stability properties with only small parasitic currents at the interface. Evidence is provided by the kinetic-energy evolution, Fig. 4(b), for an initially square droplet of size $l_x = 0.6$ and two resolutions $3h = 0.06$ and $3h = 0.03$. As a reference, we also computed the same case with the method of Hu and Adams [6], see the dashed line in the figure. At early stages, the surface-tension force produces interfacial motion deforming the square droplet, which is reflected by the peak in the logarithmic kinetic energy plot. At approximately $t = 1$ a circular droplet is formed and the particles are nearly at rest, i.e. the kinetic energy is very low. The energy-decrease at later times indicates the stability of the circular droplet configuration. Comparing our result with the simulations performed with the conservative method, good agreement is found for both resolutions. Consequently, our method neither introduces nor dissipates noticeable energy to a significant amount into the system. As the maximum velocity in the system at later times is on the order of $O(10^{-3})$ for both methods, parasitic currents are of negligible magnitude.

We also tested the square-droplet deformation with different densities for the two phases. Fig. 5 shows the pressure drop for density ratios ranging from $\Phi_\rho = \rho_1/\rho_2 = 0.001$ to $\Phi_\rho = 1000$. These ratios represent the situation of an air bubble in

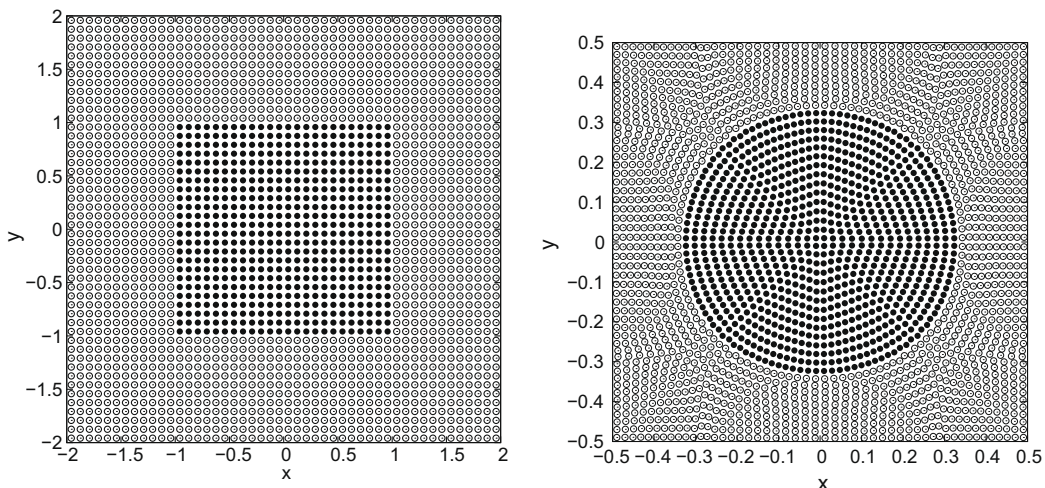


Fig. 3. Particle positions of the two fluids at (a) $t = 0$ and (b) $t = 1$.

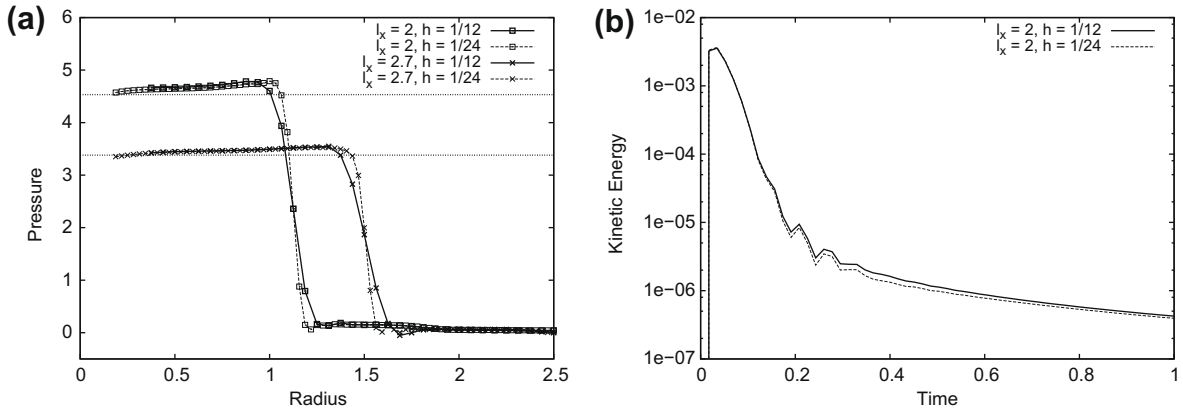


Fig. 4. Results of the simulation of the square-droplet deformation. (a) Pressure profiles vs. radial coordinate at $t = 1$ for $l_x = 0.4$ and 0.6 . (b) Temporal evolution of the kinetic energy for $l_x = 0.6$ with two different resolutions $3h = 0.06$ and 0.03 .

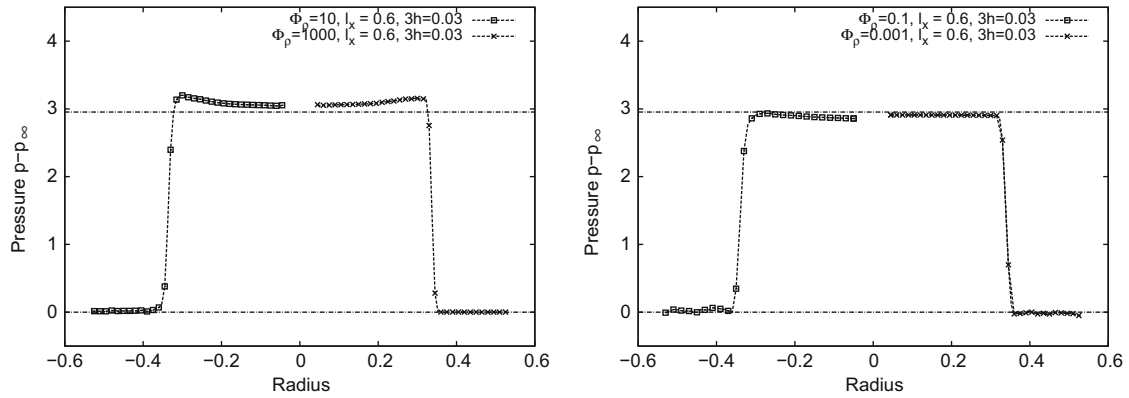


Fig. 5. Pressure drop for $l_x = 0.6$ with (a) $\phi_p = 10$ and $\phi_p = 1000$ and (b) $\phi_p = 0.1$ and $\phi_p = 0.001$.

water or a water droplet in air, respectively. Although the result is not as accurate as for the case with $\Phi_p = 1$, we find good agreement with and convergence to the analytic solution. Note that over- or underestimation of the pressure drop depends on the sign of the density gradient at the interface. This dependence can be explained by reference to the surface-tension model in our method. As we bias the surface-tension force towards the heavy phase at the interface, the approximation error implies an interface position slightly shifted towards the heavy phase.

4.2. Oscillating rod

A dynamic test case is the circular liquid-droplet oscillation under the action of capillary forces. Instead of starting from an initially elliptic droplet we prescribe an initial velocity field

$$U_x = U_0 \frac{x}{r_0} \left(1 - \frac{y^2}{r_0^2} \right) \exp \left(-\frac{r}{r_0} \right), \quad (27)$$

$$U_y = -U_0 \frac{y}{r_0} \left(1 - \frac{x^2}{r_0^2} \right) \exp \left(-\frac{r}{r_0} \right) \quad (28)$$

with $U_0 = 10$ and $r_0 = 0.05$ for the particles within the drop of radius $R = 0.2$. The computational domain is a box of size $L_x = L_y = 1.0$ and the droplet is placed at the center of the box. The densities of the liquid phase and the droplet are both set to $\rho_l = \rho_d = 1$, the dynamic viscosities are $\eta_l = \eta_d = 0.05$ and the surface-tension coefficient between the two phases is $\alpha = 1$. At the boundaries we apply no-slip wall boundary conditions. Fig. 6 shows the positions of the droplet particles at $t = 0.0, 0.08, 0.16$ and 0.26 .

To show convergence of our method we simulate the oscillating droplet with different resolutions of 900, 3600 and 14,400 particles. The result of these simulations is shown in Fig. 7(a), where we compare the position of the mass center of the particles of the upper right-quarter section of the droplet.

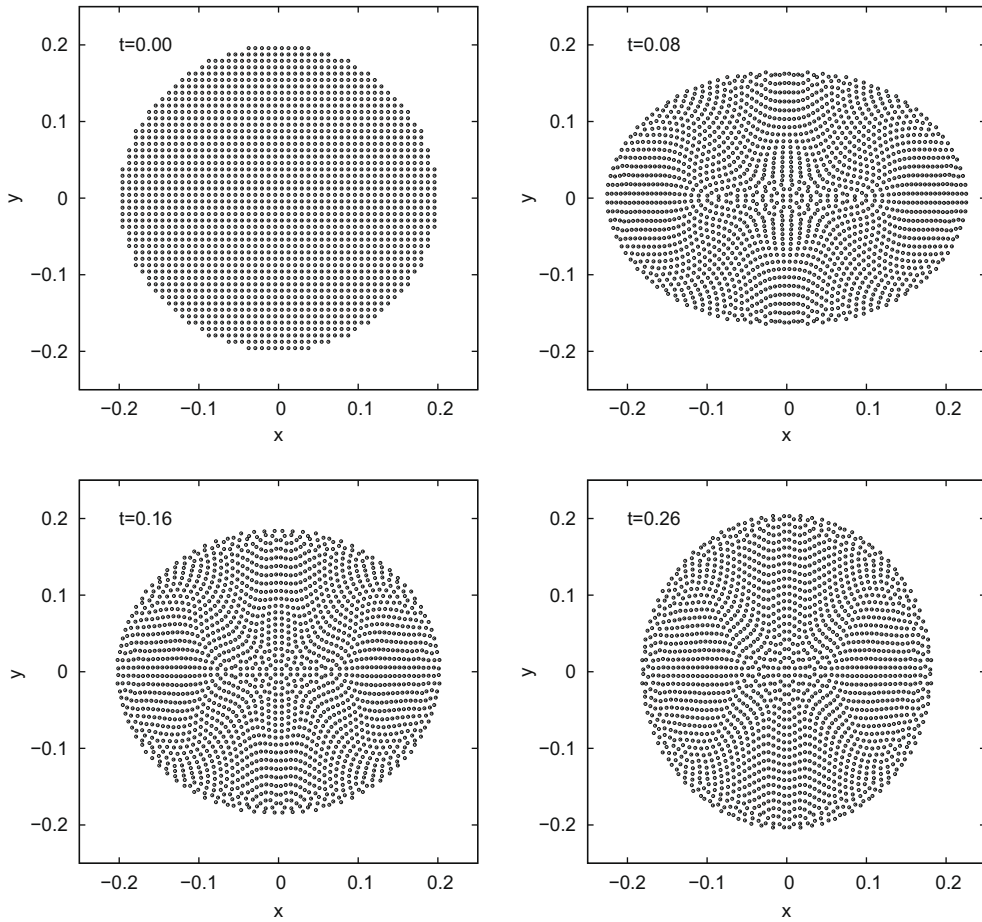


Fig. 6. Droplet oscillation with $\rho_d = \rho_l = 1$: positions of droplet particles at $t = 0.0, 0.08, 0.16$ and 0.26 .

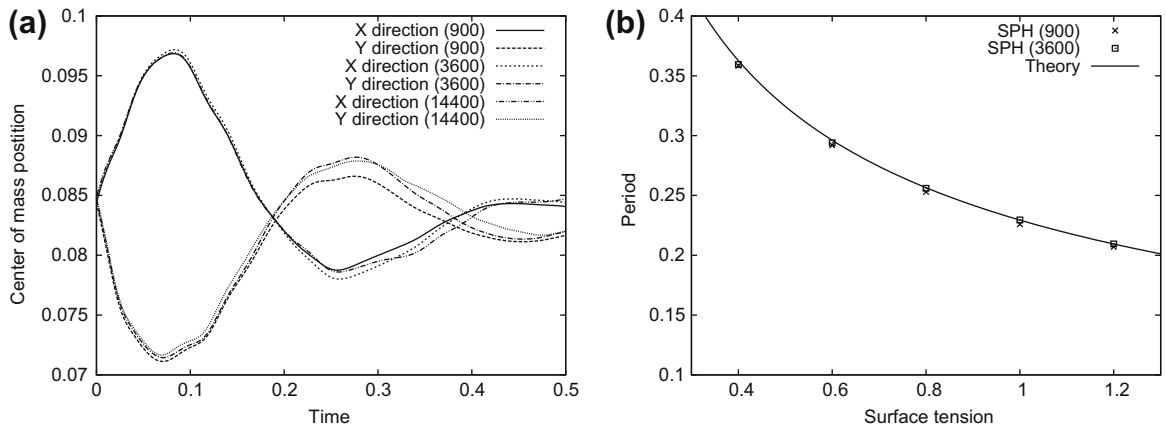


Fig. 7. (a) Droplet oscillation with $\rho_d = \rho_l = 1$: Convergence of center of mass position. (b) Droplet oscillation with $\Phi = 1000$ and $\lambda = 100$: Convergence of oscillation period.

Now we study the small-amplitude oscillations of an air–water like interface with $U_0 = 1$. For this purpose we set the density and viscosity ratio of the droplet phase and the surrounding phase to $\Phi = \rho_d/\rho_l = 1000$ and $\lambda = \eta_d/\eta_l = 100$, respectively. A study of the influence of the surface-tension coefficient on the resulting oscillation period τ is shown in Fig. 7(b). The solid line represents the theoretical relation between the surface tension α and the oscillation period $\tau = 2\pi\sqrt{\frac{R^3\rho_d}{6\alpha}}$. We find

good agreement between the analytic expression and the simulations over the entire range of studied parameters and demonstrate once again convergence of our method. As in Hu and Adams [6], the largest deviation from the theoretical values is less than 5%.

This second test case is of special importance for our new surface-tension formulation. If the simple inter-particle-averaged color gradient summation is used to obtain the curvature and normal direction, as in Hu and Adams [6], the artificial sound speed and the time-step size are determined by the surface tension and the density ratio, which leads to a much smaller Mach number (less than 0.05) and a much smaller time-step size than that obtained based on the maximum flow velocity. For the density-weighted color-gradient formulation we find that we can relax the time-step criterion implied by the surface tension (Eq. (25)) and use a suitable chosen reference density instead of the minimum density as threshold. In this example we set $\rho_{\text{ref}} = 0.1\rho_{\text{max}}$ which allows for a 10 times larger time-step as compared to ρ_{min} . The theoretical relation between the surface tension and the oscillation period can be computed accurately with a more reasonable Mach number (0.1) and significantly better efficiency, see Fig. 7(b).

4.3. Drop in shear flow

We consider a circular drop in a shear flow with a density ratio of $\Phi = 1$. The drop of size $R = 1$ is located in the middle of a periodic rectangular channel of size $L_x = L_y = 8$. A velocity of $\pm u_\infty$ is applied to the no-slip wall boundaries. The capillary number Ca and the Reynolds number Re are defined by the shear rate $G = 2u_\infty/L_y$, i.e.

$$Ca = \frac{G\eta R}{\alpha}, \quad Re = \frac{\rho GR^2}{\eta}. \quad (29)$$

In the range of parameters where a steady solution is obtained, the flow shear deforms the droplet to an ellipsoid, balancing the viscous stresses and the surface tension. As a measure of the deformation the parameter $D = (a - b)/(a + b)$ is used, which is a ratio of the transverse drop diameter a and conjugate diameter b .

Fig. 8(a) shows a snapshot of the simulation with the parameters $Ca = 0.2$, $Re = 1.0$ and a viscosity ratio of $\lambda = 100$. The calculation was performed with a smoothing length $3h = 0.25$, i.e. a total of 9216 particles. The deformation parameter is calculated with the least-square ellipse fitting method of Fitzgibbon et al. [4]. A comparison of the calculated deformations and the analytic predictions using the small-deformation theory suggested by Taylor [17] is plotted in Fig. 8(b). For both the viscosity ratios of $\lambda = 1$ and 100 we find good agreement with theory in the range of small capillary numbers. Contrary to Hu and Adams [8], the deformation parameter is slightly overpredicted, but the absolute deviation from theory using the same number of particles is smaller.

As last case we simulate a complex multi-phase problem with topology change of the interface geometry to show the capabilities of our method for technically relevant flows. For this purpose we place a three-dimensional drop of size $R = 1$ at the center of a computational domain of size $8R \times 4R \times 4R$ and move the upper and lower wall boundaries with the velocity $u_\infty = \pm 2$. Periodic boundary conditions are applied at the remaining boundaries. The shearing fluid and the drop phase have a density and viscosity ratio of $\Phi_\rho = \lambda = 1$. The other fluid properties are chosen to correspond to $Re = 1$ and $Ca = 0.25$. Fig. 9 shows the steady-state solution at $T = 25$ for a simulation with a resolution of $3h = 0.15$, i.e. a total of 1,024,000 particles. The left half of the droplet is represented with particles, the right half shows the extracted surface contour using pv-meshless [19]. The surrounding bulk phase is shown by blue particles. At $Ca = 0.25$ the shear forces are moderate compared to the surface-tension forces and the droplet deforms to a steady ellipsoid. We simulated 80,000 time-steps

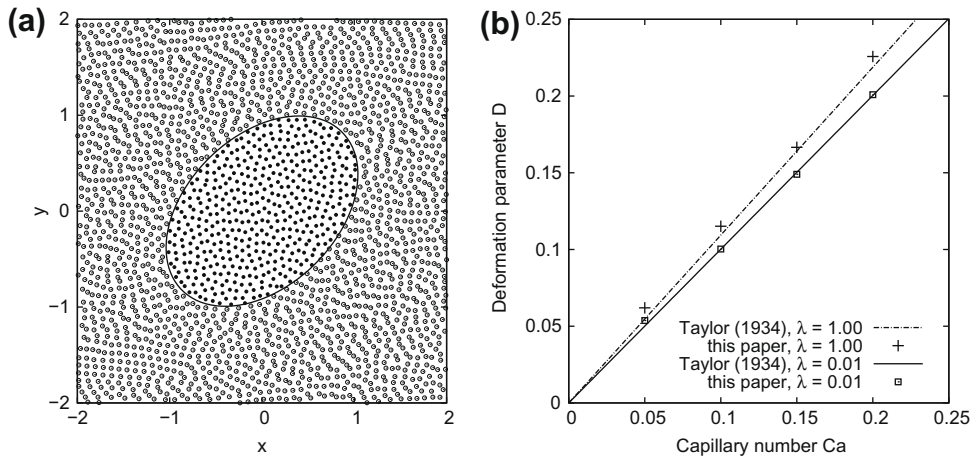


Fig. 8. (a) Positions of droplet particles and shearing fluid particles for $Ca = 0.2$, $Re = 1.0$ and $\lambda = 0.01$. (b) Drop deformation parameter D over capillary number Ca .

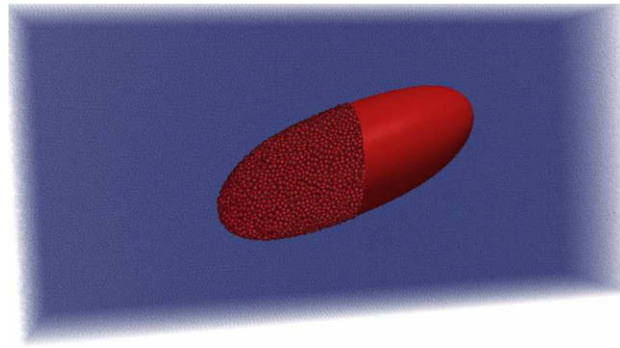
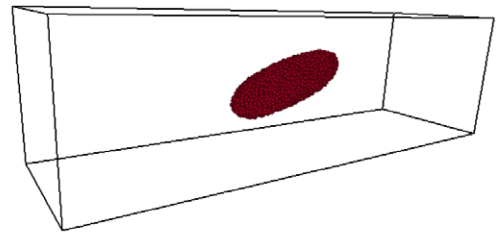
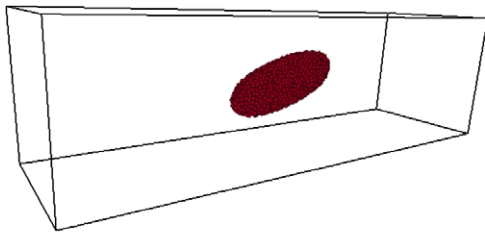
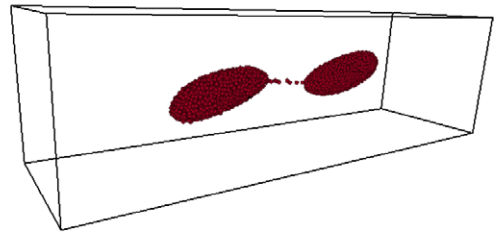
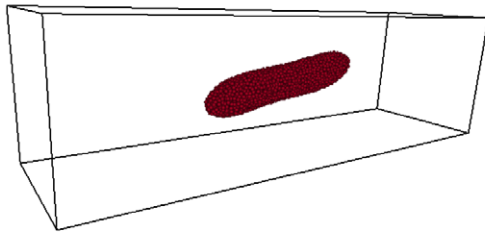


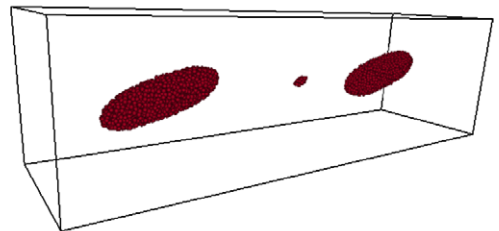
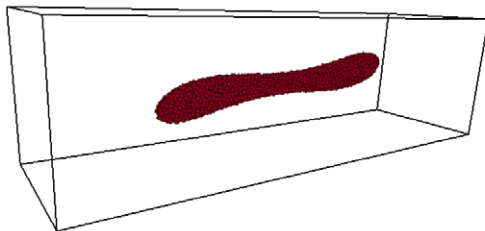
Fig. 9. Three-dimensional drop deformation in shear flow at $Re = 1$, $Ca = 0.25$ and a resolution of $3h = 0.15$ at $T = 25$.



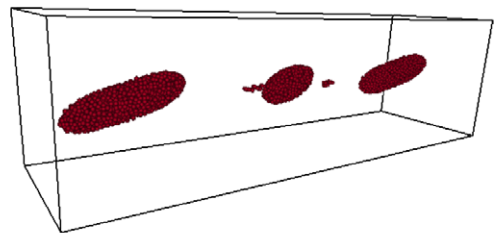
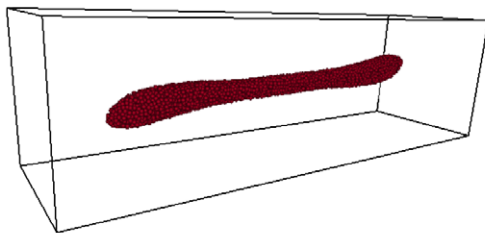
(a) $Ca=0.25$, left: $T = 25$, right: $T = 50$.



(b) $Ca=0.3$, left: $T = 25$, right: $T = 50$.



(c) $Ca=0.35$, left: $T = 25$, right: $T = 50$.



(d) $Ca=0.4$, left: $T = 25$, right: $T = 50$.

Fig. 10. Drop deformation and breakup in shear flow at $Re = 1$ and different capillary numbers at $T = 25$ (left figure) and $T = 50$ (right figure). After the breakup into two main daughter drops, the liquid thread in the middle is still unstable and separates two further small droplets.

of this example on a SGI Altix 4700 platform using 64 processors within about 80 h. The performance of the implemented SPH-client using the PPM library is about $2 \cdot 10^{-4}$ s/time-step/particle, which is comparable to the performance for a basic SPH code without surface-tension effects, see Sbalzarini et al. [15].

When the capillary number is increased, i.e. the surface-tension forces become less dominant, the capillary force is not strong enough to balance the viscous stress and no steady drop deformation is obtained. In Fig. 10 we show the results of the simulations with capillary numbers ranging from $Ca = 0.25$ to $Ca = 0.4$ in a channel of size $18R \times 4R \times 4R$ with a resolution of $3h = 0.3$. As a reference we show again the last example with $Ca = 0.25$ in Fig. 10(a). Above the critical state, see also Li et al. [9], droplet breakup occurs and produces two droplets, see Fig. 10(b). Further increasing the capillary number, the neck is more pronounced before breakup, and a very small third droplet between the other droplets is generated in Fig. 10(c). For high capillary numbers, the so-called “dumbbell” shape has a very long neck and a more complex breakup process occurs. In Fig. 10(d) we show that at $Ca = 0.4$ five droplets occur.

This example shows quite clear one advantage of SPH (and particle methods in general) compared to grid-based methods in studying multi-phase problems: once the studied problem is initialised, by its nature the method incorporates interface phenomena adaptively, i.e. the change of the interface geometry or even separation and merging are handled without the need of special numerical algorithms.

5. Concluding remarks

In this work, we present a novel surface-tension method for multi-phase SPH. With a new reproducing divergence approximation, we propose a new formulation for the surface curvature and modify the color gradient summation with a density weighting. While the new formulation has comparable accuracy as the formulation of Hu and Adams [6], it can achieve much faster computation for problems with large density ratio. Although demonstrated here only for the case of two different fluids distinguished by a single color function, we emphasize that an extension to handle more complex multi-phase problems is straightforward. We have validated our method with analytic solutions for steady equilibrium droplets, capillary waves and drop deformations in shear flow. We demonstrate convergence of our method and good stability properties even for long time simulations. The simulation of a complex three-dimensional problem shows the capabilities of our method in handling multi-phase problems with complex interfaces.

Acknowledgment

The authors wish to acknowledge the support of the German Research Foundation (DFG – Deutsche Forschungsgesellschaft) for funding this work within the project AD 186/6-1.

References

- [1] J.U. Brackbill, D.B. Kothe, C. Zemach, A continuum method for modeling surface tension, *J. Comput. Phys.* 100 (2) (1992) 335–354.
- [2] J.K. Chen, J.E. Beraun, T.C. Carney, A corrective smoothed particle method for boundary value problems in heat conduction, *Int. J. Numer. Methods Eng.* 46 (2) (1999) 231–252.
- [3] P. Español, M. Revenga, Smoothed dissipative particle dynamics, *Phys. Rev. E* 67 (2) (2003) 026705.
- [4] A. Fitzgibbon, M. Pilu, R.B. Fisher, Direct least square fitting of ellipses, *IEEE Trans. Pattern Anal. Machine Intell.* 21 (1999) 476–480.
- [5] J. Hongbin, D. Xin, On criterions for smoothed particle hydrodynamics kernels in stable field, *J. Comput. Phys.* 202 (2) (2005) 699–709.
- [6] X.Y. Hu, N.A. Adams, A multi-phase SPH method for macroscopic and mesoscopic flows, *J. Comput. Phys.* 213 (2) (2006) 844–861.
- [7] X.Y. Hu, N.A. Adams, Angular-momentum conservative smoothed particle dynamics for incompressible viscous flows, *Phys. Fluids* 18 (10) (2006) 101702.
- [8] X.Y. Hu, N.A. Adams, An incompressible multi-phase SPH method, *J. Comput. Phys.* 227 (1) (2007) 264–278.
- [9] J. Li, Y.Y. Renardy, M. Renardy, Numerical simulation of breakup of a viscous drop in simple shear flow through a volume-of-fluid method, *Phys. Fluids* 12 (2) (2000) 269–282.
- [10] J.J. Monaghan, Smoothed particle hydrodynamics, *Rep. Prog. Phys.* 68 (8) (2005) 1703–1759.
- [11] J.P. Morris, Simulating surface tension with smoothed particle hydrodynamics, *Int. J. Numer. Methods Fluids* 33 (3) (2000) 333–353.
- [12] J.P. Morris, P.J. Fox, Y. Zhu, Modeling low reynolds number incompressible flows using SPH, *J. Comput. Phys.* 136 (1) (1997) 214–226.
- [13] S. Nugent, H.A. Posch, Liquid drops and surface tension with smoothed particle applied mechanics, *Phys. Rev. E* 62 (4) (2000).
- [14] P.W. Randles, L.D. Libersky, Smoothed particle hydrodynamics: some recent improvements and applications, *Comput. Methods Appl. Mech. Eng.* 139 (1–4) (1996) 375–408.
- [15] I.F. Sbalzarini, J.H. Walther, M. Bergdorf, S.E. Hieber, E.M. Kotsalis, P. Koumoutsakos, PPM – a highly efficient parallel particle-mesh library for the simulation of continuum systems, *J. Comput. Phys.* 215 (2) (2006) 566–588.
- [16] A.M. Tartakovsky, P. Meakin, Modeling of surface tension and contact angles with smoothed particle hydrodynamics, *Phys. Rev. E* 72 (2) (2005).
- [17] G.I. Taylor, The formation of emulsions in definable fields of flow, *Proc. Roy. Soc. London Ser. A* (1934) 501–523.
- [18] Y. Zhu, P.J. Fox, Smoothed particle hydrodynamics model for diffusion through porous media, *Transport Porous Media* 43 (3) (2001) 441–471.
- [19] J. Biddiscombe, D. Graham, P. Maruzewski, Interactive visualization and exploration of SPH data, in: *Proceedings of 2nd SPHERIC international workshop*, Madrid (Spain), May 2007, pp. 47–50.